Simultaneous PLIF/PIV Investigation of Vortex-Induced Annular Extinction in H_2-Air Counterflow Diffusion Flames

T. R. Meyer, G. J. Fiechtner, S. P. Gogineni, J. C. Rolon, C. D. Carter, J. R. Gord

T. R. Meyer, S. P. Gogineni
Innovative Scientific Solutions, Inc.
2766 Indian Ripple Road
Dayton, OH 45440, U.S.A.

G. J. Fiechtner
Sandia National Laboratories
7011 East Avenue, MS9951
Livermore, CA 94550, U.S.A.

J. C. Rolon
Laboratoire E.M2.C, CNRS/École Centrale Paris
92295 Chatenay-Malabry Cedex, France

C. D. Carter, J. R. Gord
Air Force Research Laboratory
Wright-Patterson Air Force Base, OH 45433, U.S.A.

Abstract High-temporal-resolution measurements of scalars and velocity are used to study vortex-induced annular (off-centerline) flame extinction during the interaction of a propagating vortex with an initially stationary counterflow hydrogen-air diffusion flame. Such an extinction process differs from classical one-dimensional descriptions of strained flamelets in that it captures the effects of flame curvature as well as dynamic strain. Planar laser-induced fluorescence (PLIF) measurements of the hydroxyl radical (OH) are used to track flame development, and simultaneous particle-image velocimetry (PIV) is used to characterize the two-dimensional flowfield. Measurements reveal differences in local normal strain rate profiles along and across the reaction zone and indicate that vortex-induced curvature in the annular region may initiate the extinction process. Conversely, the effect of local flame extinction on vortex evolution and dissipation is determined from measured vorticity data.

1

Introduction

It is well recognized that vortices occur readily in turbulent flows. Recent laser-based measurements of species and velocity in turbulent diffusion flames have revealed that vortical structures play a significant role in local flame extinction, curvature, thickness, and stabilization (Watson et al. 1999, Donbar et al. 2001). Detailed studies of vortical structures in fully turbulent flames are difficult because those structures must be tracked in both space and time with respect to the flame front. Alternatively, fundamental turbulent flame behavior can be represented by the interaction of a laminar, non-premixed flame with a repeatable, spatially propagating toroidal vortex (Rolon et al. 1995, Samaniego and Mantel 1999). The resulting data can be used to investigate the effects of unsteady strain and curvature or to identify fundamental regimes of vortex-flame interaction (Katta

et al. 1998, Fiechtner et al. 1999, Renard et al. 2000, Thévenin et al. 2000, Katta et al. 2003, Lemaire et al. 2003).

While extinction in such vortex-flame studies has typically been observed to take place at a point located at the leading edge of the vortex, Katta et al. (1998) predicted that flame extinction can occur in an annular pattern away from the centerline under certain experimental constraints. Experimental observation of this annular extinction was first reported in a collaborative publication between scientists at the Air Force Research Laboratory and École Centrale Paris (Thevenin et al. 2000), with a view toward establishing various regimes of vortex-induced wrinkling and extinction. The current work focuses on the annular extinction itself as an archetype for flamelet bahavior under the influence of two-dimensional flowfields. Thus, the current investigation of off-centerline extinction emphasizes flame dynamics induced by vortex rotation in addition to flow unsteadiness. We provide a detailed description of the experimental apparatus used to observe the annular extinction and present possible reasons for its occurrence. In addition, we examine the effects of flame extinction or the lack thereof on the vorticity magnitude and discuss the degree of coupling between the flame front and vortex flowfield.

These goals are accomplished using detailed measurements of the time-dependent velocity and concentration fields in a non-premixed flame supported by air and fuel in a counterflow burner configuration (Rolon et al. 1995). Here, a piston is used to inject vortices of varying strength, and the hydrogen fuel is diluted with nitrogen at various levels to study the effect of global mixture ratio. Planar laser-induced fluorescence (PLIF) of the hydroxyl radical (OH) is used to mark the flame front, and two-color particle-image velocimetry (PIV) is employed to characterize the vortex structure. Recently, several researchers have conducted a number of joint PLIF/PIV experiments in unsteady flames. Rehm and Clemens (1997) have made OH-PLIF and PIV measurements in a

hydrogen jet flame. Joint scalar and velocity-field measurements were performed by Frank et al. (1996), Donbar et al. (2001), and Kothnur et al. (2002) in turbulent flames and by Hasselbrink and Mungal (1998) and Watson et al. (1999, 2002) in lifted methane-air diffusion flames. The present simultaneous OH-PLIF and PIV measurements are the non-premixed counterpart of the vortex-flame studies of Driscoll et al. (1994) and Mueller et al. (1995). To explore the time-dependent nature of the vortex-flame interactions, a synchronization scheme for precise control of relative timing between the laser diagnostics and vortex-flame event is also implemented. A temporal resolution of 10 μs is achieved with this scheme, allowing the annular extinction to be observed at various phases of its evolution.

2

Experimental Method

2.1

Counterflow Burner

Several experimental facilities have been implemented to study vortex-flame interactions, as reviewed by Renard et al. (2000). For the experiments described in this paper, a vortex is injected into a flame supported at the mid-plane of an opposed-jet burner (Rolon et al. 1995) with 25-mm-diameter upper and lower nozzles separated by 40 mm. A diagram of the burner is shown in Fig. 1. The fuel, consisting of hydrogen diluted with nitrogen, flows from the upper nozzle; air flows from the lower nozzle. This configuration differs from conventional counterflow flames in that a tube with 5-mm inner diameter is installed concentrically within the lower nozzle. This tube is attached to a cylinder containing a solenoid-driven piston that forces a vortex to emerge from the tube and collide with the flat counterflow flame.

Since vortex formation in non-reacting flow has been the subject of intense study for many years, a considerable amount of information is available to aid in characterizing the injected vortices. As fluid is pumped impulsively from a nozzle or orifice, a single vortex forms, followed by additional vortices in the production of a starting jet (Garside et al. 1943). For a cylindrical volume of fluid that emanates from a nozzle having length L and diameter D, Gharib et al. (1998) and Shusser et al. (1998) have shown that the maximum circulation attainable by a vortex ring is reached for $L/D \sim 4$ and that for larger ratios additional trailing vortex rings form. For the present 5-mm nozzle, the volume that a vortex can contain, as estimated from the results of Gharib et al., is ~0.4 cm^3. The vortex generator used in the present study can sweep a maximum volume of ~2.5 cm^3, for a maximum attainable L/D ratio of ~25. For the experiments described here, comparatively strong vortices are generated using a 10-ms piston rise time.

Since the aim of the present study is to produce vortex-flame events that are similar to those achieved in the computations of Katta et al. (1998), the piston is allowed to travel through its maximum range, but the tube is placed such that the diagnostics are triggered before additional vortices exit the tube. Models that rely on an artificially created vortex pair by specifying the vortex field (Ashurst 1993, Poinsot et al. 1987, and Rutland et al. 1991) may not be well represented by our experimental conditions because of the geometry and vorticity field associated with a time-evolving pulsed jet. A detailed discussion of vortex formation in our apparatus is given elsewhere (Fiechtner et al. 2000a and Fiechtner et al. 2000b), with emphasis on the importance of matching experimental conditions and boundary conditions during comparison of experimental data and model predictions.

Vortex conditions are monitored carefully to avoid multiple-vortex or turbulent conditions by examining scattering images that are acquired with a charge-coupled device (CCD) camera. Vortex visualization is accomplished during alignment of the vortex nozzle using PLIF of acetone

(Fiechtner et al. 1998); a vaporizer is installed temporarily between the vortex tube and the mass-flow controller for this purpose. Because acetone changes the fuel content and character of the counterflow flames, this visualization is only performed to determine the non-reacting vortex properties.

The laminar vortices produced experimentally travel upward within the surrounding oxidizer flow. A flow of air is supplied to the vortex tube such that in the absence of a vortex, the exit velocity matches the velocity of the air emanating from the surrounding nozzle. To minimize the impact of room-air disturbances, upper and lower guard flows of nitrogen are supported through outer nozzles, which are concentric with the respective upper (fuel) and lower (air) inner nozzles. The hydrogen, nitrogen-diluent, and air flows are furnished by mass-flow controllers with respective full-scale ranges of 20, 20, and 30 l/min. A continuous flow of air is provided to the vortex tube by a 5-l/min controller, while the guard flows for the upper and lower guard (outer) nozzles are furnished by two 50-l/min mass-flow controllers. The flow rates of the controllers are accurate to ±1% of the full-scale range. The experiments have been repeated for three flame conditions (Table 1).

Seed particles are introduced into the burner flows when digital PIV measurements of the vortex velocity are performed. Three particle seeders are installed—one after the air mass-flow controller, a second after the vortex-air mass-flow controller, and a third after the junction where the hydrogen and nitrogen gases are mixed. Each flow is seeded with hollow spherical ceramic particles with an approximate mean diameter of 2.4 μm. PLIF experiments are also performed with unseeded flows to ensure that there are no significant differences with results from experiments with seeded flows.

2.2

PLIF/PIV System

A review of PLIF fundamentals can be found in Eckbreth (1988). The PLIF system in the current experiment contains a frequency-doubled, Q-switched Nd:YAG laser that is used to pump a dye laser; this dye laser, in turn, is frequency doubled. The UV radiation is directed through a telescope that is adjusted to produce a light sheet with a height that matches as nearly as possible the 40-mm burner separation. The resulting beam thickness is ~300 μm, which corresponds to the full width (defined as the distance between the locations of the 25%-peak-intensity points).

Hydroxyl radicals absorb the laser radiation at 281.3nm via the $R_1(8.5)$ transition of the (1,0) band in the A-X system. For flame temperatures ranging from 1100-2200K, the Boltzmann population fraction for this transition varies by only 10%. Thus, large changes in OH PLIF signal within this temperature range can be attributed to changes in OH number density rather than changes in the Boltzmann population fraction for the $R_1(8.5)$ transition. The OH PLIF signal is expected to drop significantly below 1100K and mark flame extinction both because of a drop in the Boltzmann population fraction for the $R_1(8.5)$ transition and because chemical reactions are expected to cease below this temperature (Renard et al. 1999, Rolon et al. 1996).

After laser excitation of the $R_1(8.5)$ transition, fluorescence from the A-X (1,1) and (0,0) bands is detected normal to the laser sheet through Schott WG-295 and UG-11 colored-glass filters using a 105-mm-focal-length f/4.5 UV lens. The resulting UV fluorescence is recorded on an intensified CCD camera with an intensifier gate width of 100 ns. CCD pixels are binned in 2 x 2 groups; the result is an effective array size of 288 x 192 pixels, with an imaged area of 25.6 x 38.4 mm^2. The bottom of the image is flush with the surface of the lower nozzle. A color table is used, with a maximum value set to 100% of the maximum signal for each image. The low-signal color of 10% is

at least two standard deviations above the mean background. Therefore, in cases where "extinction" of the OH layer is observed, this term refers to signal levels that fall below this minimum value and are thus assigned the last color in the table.

In studies of vortex-flame interactions conducted by other investigators (see, for example, Najm et al. 1998 and Paul et al. 1998), LIF was assumed to mark a quantity such as heat release or burning rate. In the present experiments OH images are obtained for the direct comparison of certain spatial and temporal features and for comparison with the flame structure predicted by Katta et al. (1998); therefore, no attempt is made to correlate the images with other quantities, although it has been shown recently that the OH concentration may be a good indicator of flame extinction in this configuration (Renard et al. 1999). This is confirmed experimentally through qualitative Rayleigh scattering images under similar conditions, although no attempt is made to determine the exact moment of flame extinction due to the added uncertainty of increased OH fluorescence quenching at depressed temperatures.

An introduction to PIV can be found in Raffel et al. (1998). Measurements of the velocity field in the current work are carried out using digital two-color PIV (Gogineni et al. 1998). A color digital CCD with an array of 3060 x 2036 pixels is used with an imaged area of 26.0 x 39.0 mm^2 (roughly matching the PLIF field of view). The color CCD camera for PIV and the intensified CCD array for OH PLIF are aligned using a transparent mask printed with a graduated scale. Further alignment between images is performed after each experiment in post-processing; a transformation in two-dimensional space is applied to the PIV images relative to the PLIF images resulting in a final viewing area of 24.5 x 36.0 mm^2. Two lasers are employed, with one PIV light sheet being produced by frequency doubling the output of a Q-switched Nd:YAG laser (30 mJ/pulse at the test section). The remainder of this beam is used to pump the dye laser that is frequency doubled to

excite OH. The second PIV light sheet is produced by pumping a dye laser (employing DCM laser dye) with a second frequency-doubled, Q-switched Nd:YAG laser; this results in laser radiation at 640 nm (40 mJ/pulse at the test section). The thickness of both the red and the green light sheets is set to ~700 μm in the probe region. Due to the size and axisymmetric geometry of the vortex flowfield, significant gradients are not expected across this laser-sheet thickness. A digital delay generator is used to drive the timing of the two lasers such that the red pulses are delayed precisely with respect to the green ones. In the absence of a vortex, the underlying counterflow velocity field is probed with red pulses that are delayed by up to 1 ms with respect to the corresponding green pulses. For the most rapid vortices studied, the delay between red and green pulses is reduced to 10 μs. The camera shutter is set to open for 1/15 s to permit detection of both laser pulses by the color CCD while minimizing interferences from flame emission and ambient light.

Velocity vectors are calculated using custom-designed software developed at Stanford (StanPIV – Hasselbrink 1999). This software incorporates several improvements to standard (single-pass) PIV algorithms and allows recursive estimation of the velocity field. A correlation area of 32×32 pixels is used in the calculation, corresponding to a correlation area of 0.067 cm^2 and a spatial resolution of 400 μm. The latter corresponds to four or five vectors across the unpurturbed OH layer. Spurious vectors are filtered using a consistency filter that rejects vectors for which the square root of $(\Delta x_i - \Delta x_o)^2 + (\Delta y_i - \Delta y_o)^2$ is greater than about one-tenth of the distance across an interrogation region for three of the eight nearest neighbors. Here, Δx and Δy are the cross-correlation distances, the subscript "i" denotes the eight nearest neighbors, and the subscript "o" denotes the vector being filtered. The values of the vectors that are invalidated by the filter are interpolated.

2.3

High-Temporal-Resolution Synchronization Scheme

Because data on the time-dependent nature of the vortex-flame interactions are to be analyzed in conjunction with simultaneous scalar and velocity data, precise synchronization of several experimental events is required. These events include the generation and propagation of vortices, production of laser pulses, and activation of the PIV-camera shutter and PLIF-camera intensifier. As explained in the following discussion, the current synchronization scheme, shown in Fig. 2, was developed in order to avoid the inherent jitter caused by long term delays in conventional delay generators. This problem arises when trying to synchronize the 0.5-s delay of piston actuation from an arbitrary-waveform generator (AWG) to the 5th pulse of a 10-Hz laser trigger from a digital delay generator (DDG). The jitter between 10-Hz clock outputs is one part in 10^4, corresponding to a jitter of 50 μs over the 0.5-s period. For this reason, attempts to synchronize the piston and 10-Hz clock severely limit the temporal resolution available to "freeze" the vortex-flame events and require an intensifier gate width larger than 50 μs (which leads to an unacceptable level of background flame emission).

When the DDG is triggered externally, however, the jitter between the trigger and a delayed DDG output pulse is 60 ps plus the output delay divided by 10^8. Over the 0.5-s period between the first and fifth laser pulses, this corresponds to a jitter of only 5 ns. Thus, a 10-Hz clock is added to the system for driving the lasers, and an externally triggered master DDG is used to impose a low-jitter 0.5-s delayed pulse, which pre-empts the fifth pulse of the 10-Hz clock (note the 50-Ω power combiner in Fig. 2). This approach reduces the jitter in the timing of the fifth laser pulse from 50 μs to <10 ns while maintaining the nominal 10-Hz repetition rate required by the lasers. The

coincidence unit in Fig. 2 ensures that pre-emptive triggering occurs only when an initiation pulse is output from the PLIF camera controller.

Other outputs of the master DDG are delayed suitably and directed to the image detectors. For PIV experiments, the width of a TTL pulse is adjusted using a gate generator that closes a relay to trigger the digital PIV camera system. For simultaneous PLIF experiments, another master-DDG output triggers a pulse generator that, in turn, activates the intensifier of an ICCD camera.

The scheme depicted in Fig. 2 provides precise control of the relative timing between the laser diagnostics and the vortex-flame event. To explore the temporal evolution of the event, data are captured utilizing the following phase-locked timing sequence: 1) an image is recorded, 2) the delay between vortex production and the laser/camera events is adjusted, and 3) another vortex is initiated and a second image recorded. This process is repeated to acquire numerous images that are obtained at increasing delays. An animation is then created by assembling the individual images in temporal order.

3

Results and Discussion

The temporal sequence of OH PLIF images during an annular extinction is shown in Fig. 3 for Flame A in Table 1. The temporal delay between images is 10 μs, and the vortex velocity is 11.5 m/s. The off-centerline break in the OH layer shown in these figures is very similar in structure to that observed numerically by Katta et al. (1998), attesting to the predictive capability of their code. The 10-μs temporal delay used to resolve the extinction process demonstrates the success of the synchronization scheme for repeatable imaging of high-speed vortices and is similar to that employed in the computations. In the following discussion, we present PLIF/PIV data for cases with

and without flame extinction to highlight various features of the vortex-flame interaction process. We then present more detailed calculations of the normal strain field and discuss the annular extinction in greater detail.

Simultaneous images of OH PLIF overlaid with instantaneous velocity vectors from PIV are shown in Figs. 4 and 5 for cases with no flame extinction (weaker vortex) and with flame extinction (stronger vortex), respectively. Inflow conditions match those of Flame C in Table 1. Each OH PLIF image is normalized to the peak signal level within the unperturbed region of the flame. The velocity vectors plotted here correspond to the reference frame of the vortex and are obtained by subtracting its convection velocity. The number of vectors is reduced by 60% for presentation purposes. Figures 4 and 5 also show vorticity distributions computed by central differencing of the velocity field.

For the case with no flame extinction, shown in Fig. 4, the vortex velocity is about 4 m/s, and images are separated by 9 ms. As the vortex approaches, the flame surface becomes highly wrinkled and wraps around the leading edge of the vortex. The flame then burns across the vortex rollers without being extinguished and continues propagating along the vortex column, as shown in the central and right-most frames of Fig. 4a. The location of the vortex structure is shown more clearly in the vorticity plots of Fig. 4b. The case with flame extinction is shown in Fig. 5, with a time spacing between frames of 6 ms. The vortex shown in Fig. 5a breaks the OH layer as it advances toward the upper nozzle, after which the flame propagates into the vortex rollers and begins to reconnect.

The following is a frame-by-frame comparison of Figs. 4 and 5 to illustrate the effect of flame extinction on the vortex flowfield. The plot of vorticity in the left-most frame of Fig. 5b shows that the vortex is stronger than that of Fig. 4b. As a consequence, the vortex in the central frame of Fig. 5b induces a local flame extinction and is able to sustain its rotation. By comparison, the vortex in

the central frame of Fig. 4b is dissipated because of interaction with the flame and a corresponding increase in viscosity for the combustion products. In the right-most frame of Fig. 5b, however, the locally quenched flame begins to reconnect, and the overtaken vortex is even more strongly dissipated than the vortex of Fig. 4b. This suggests that the laminarization of local turbulence in non-premixed flames can be achieved through different mechanisms for vortices of varying strength, with reconnection playing a significant role for vortices that are strong enough to induce a local flame extinction.

Details of the flame extinction process are not evident in Fig. 5 because of the relatively large time spacing between images. To explore this process in more detail, simultaneous OH PLIF and velocity vectors are plotted in Fig. 6 for three images during the interaction of an 8.25-m/s vortex with Flame B from Table 1. The flame begins to thin in an annular region as the vortex approaches in the left-most frame, and is followed by a clear break in the OH layer in the central frame. Regions I-III in Fig. 6 are located 0-10 mm along the OH layer, with the centerline (Region I) located at 0 mm and the annulus (Region II) located at about 5 mm.

Figure 7a contains line plots of the relative OH PLIF signal and velocity gradient normal to the flame surface, dU_n/dR; data are from the left-most image of Fig. 6, where U_n and R are the velocity and spatial components, respectively, normal to the flame surface. From this definition, dU_n/dR represents the compressional-strain component across the flame. The abscissa of Fig. 7a represents the distance *along* the center of the OH layer from Region I to Region III. The velocity gradient is calculated using a combination of central differencing and linear interpolation between grid points. Increasing the vector density by a factor of two did not significantly alter the measured strain rates, indicating that the velocity gradients are adequately resolved by the 32×32 interrogation regions used here. Based on noise in the velocity data, the uncertainty in measured strain rates is estimated

to be ±10%. In Fig. 7a, where strain rates are plotted with respect to the OH layer, errors in PIV/OH image registration lead to a final uncertainty of about ±15%. In terms of shot-shot fluctuations in vortex strength and trajectory, these strain rate measurements are considered to be repeatable to within ±25%.

According to the plot of relative OH signal in Fig. 7a, flame extinction begins to occur near Region II in an annular region away from the jet centerline and within a region of maximum dU_n/dR. By reviewing the left-most image of Fig. 6, it is clear that this off-axis compressional strain is induced by the tangential velocity of the rotating vortex. To further compare the strain rates acting upon the flame in the centerline and annular regions, line plots of dU_n/dR *across* the flame in Regions I and II, respectively, are shown in Fig. 7b for comparison. Unlike in Fig. 7a, the asbcissa of Fig. 7b represents the distance from the center of the OH layer. The value of dU_n/dR toward the *fuel side* of the OH layer is slightly higher in the annular region than at the centerline, with measured peak values that are within 10% of those predicted by Katta et al. (1998). In contrast, the experimental and computed *air-side* strain rates are lower at the annulus than at the centerline. The spatially integrated strain rate across the flame is also about 10-15% lower at the annulus than at the centerline. Uncertainties in the velocity measurements due to thermophoresis (Sung et al. 1996) are not expected to significantly alter this analysis because strain rates are reported relative to the OH layer and, presumably, relative to an isocontour of temperature.

These data indicate that the local strain rate may not be the controlling parameter in the initiation of annular flame extinction. Katta et al. (1998) argued instead that the annular extinction may result from increased local curvature and preferential diffusion. It is apparent from the central frame of Fig. 6, for example, that flame extinction is initiated in Region II near a location of maximum curvature. By fitting the flame profile along 5-mm sectors at the centerline and annulus,

the radius of curvature for each region was calculated to about 10 mm and 5 mm, respectively, to within ±5%. Due to higher curvature in the annular region, thermal diffusion per unit area is reduced on the fuel side by a factor of four as compared with the centerline region, while preferential diffusion of hydrogen would bring an influx of cool, fuel-rich gases into the annular flame zone and depress the reaction rate. In contrast with the flame structure of Fig. 6 noted above, the leftmost of images of the non-extinguished flame of Fig. 4a show no apparent increase in curvature in the annular region. Correspondingly, the flame in Fig. 4a is slightly thinner at the centerline than at the annulus, further indicating that local variations in curvature may play a dominant role in the initiation of flame extinction for the current flow regime.

4

Conclusions

The interaction of a toriodal vortex with a flat, counterflow, hydrogen-air diffusion flame captures a number of important processes in turbulent combustion, including vortex-induced flame wrinkling, stretch, normal strain, and unsteadiness. To first order, centerline flame extinction at the leading edge of the vortex simulates the effects of unsteadiness and flame stretch. In the current study, off-centerline strain rates and curvature induced by the rotational component of the approaching vortex were determined using simultaneous OH PLIF and PIV. Analysis of local normal strain rates *along* the OH layer shows slightly higher magnitudes near the annular region where flame extinction is first observed, but measurements across the flame show a more complex strain rate distribution. In contrast, high local curvature in the annular region is shown to correlate well with the initiaion of flame extinction. To assess the effects of flame extinction on the flowfield, plots of vorticity calculated from the PIV data are used to show that the case with flame extinction has higher initial vortex strength but experiences greater levels of dissipation at later times during flame reconnection.

Thus, the ability to obtain measurements of scalars and velocity in a time-correlated sequence is demonstrated to be particularly useful in studying the coupled effects of fluid dynamics and flame chemistry in dynamically strained, curved flamelets. Such conditions more closely simulate the fluid-chemistry interactions that are typical in turbulent diffusion flames.

Acknowledgments

The authors thank Dr. W. M. Roquemore, Dr. V. R. Katta, Dr. P. H. Renard, and Prof. D. Thévenin for guidance and valuable discussions. The authors also thank Dr. R. D. Hancock and Capt. I. Vihinen for assistance in assembling the burner and Mr. K. D. Grinstead and Dr. J. M. Donbar for technical assistance in setting up the experiments. Finally, the authors thank Prof. G. Mungal of Stanford University for providing the StanPIV software. This work was supported by U. S. Air Force Contracts F33615-95-C-2507, F33615-97-C-2702, and F33615-00-C-2608. Additional funding was provided by the U.S. Air Force Office of Scientific Research with Dr. Julian Tishkoff as Program Manager.

References

Ashurst WT (1993) Combust Sci Technol 92:87

Croonenbroek T (1996) Doctoral thesis, Laboratoire E.M2.C, CNRS and École Centrale Paris

Donbar JM; Driscoll JF; Carter CD (2001) Combust Flame 125(4):1239-1257

Driscoll JF; Sutkus DJ; Roberts WML; Post ME; Goss LP (1994) Combust Sci Technol 96:213-229

Eckbreth AC (1996) Laser diagnostics for combustion temperature and species, 2nd Ed. Gordon and Breach Publishers, The Netherlands.

Fiechtner GJ; Carter CD; Katta VR; Gord JR; Donbar JM; Rolon JC (1999) Regimes of

interaction between a nonpremixed hydrogen-air flame and an isolated vortex. AIAA Paper 99-0320

Fiechtner GJ; Katta VR; Carter CD; Gord JR; Roquemore WM; Rolon JC (2000a) J Visualization 3:96

Fiechtner GJ; Renard PH; Carter CD; Gord JR; Rolon JC (2000b) J Visualization 2(3/4):331-342

Fiechtner GJ; Carter CD; Grinstead KD; Gord JR; Roquemore WM; Rolon JC (1998) Flame-vortex interactions in a non-premixed H_2/N_2/air counterflow burner. AIAA Paper 98-3770

Frank JH; Lyons KM; Long MB (1996) Combust Flame 107:1-12

Garside JE; Hall AR; Towsend DTA (1943) Nature 152:748

Gharib M; Rambod E; Shariff K (1998) J Fluid Mech 360:121-140

Gogineni S; Goss L; Pestian D; Rivir R (1998) Exp Fluids 25:320-328

Hasselbrink E (1999) Transverse jets and jet flames: structure, scaling, and effects of heat release. Doctoral thesis, Stanford University, Stanford, CA

Hasselbrink EF; Mungal MG (1998) Proc Combust Inst 27:1167-1173

Katta VR; Carter CD; Fiechtner GJ; Roquemore WM; Gord JR; Rolon JC (1998) Proc Combust Inst 27:587-594

Katta VR; Meyer TR; Gord JR; Roquemore WM (2003) Combust Flame 132:639-651

Kothnur PS; Tsurikov MS; Clemens NT; Donbar JM; Carter CD (2002) Proc Combust Inst 29: in press

Lemaire A; Meyer TR; Zähringer K, Rolon JC, Gord JR (2003) Appl Opt 42(12): 2063-2071

Mueller CJ; Driscoll JF; Sutkus DJ; Roberts WL; Drake MC; Smooke MD (1995) Combust Flame 100:323-331

Najm HN; Paul PH; Mueller CJ; Wyckoff PS (1998) Combust Flame 113:312-332

Paul PH; Najm HN (1998) Proc Combust Inst 27:43-50

Poinsot T; Trouve A; Veynante D; Candel S; Esposito E (1987) J Fluid Mech. 177:265-292

Raffel M; Willert C; Kompenhans J (1998) Particle image velocimetry: a practical guide. Springer Verlag

Rehm JE; Clemens NT (1998) Proc Combust Inst 27:1113-1120

Renard P-H; Rolon JC; Thévenin D; Candel S (1999) Combust Flame 117:189-205

Renard PH; Thevenin D; Rolon JC; Candel S (2000) Prog Energy Combust Sci 26:225-282

Rolon JC; Aguerre F; and Candel S (1995) Combust Flame 100:422-429

Rolon JC; Darabiha N Croonenbroek T; Dagusé Th; Martin JP (1996) Quantitative LIF and Rayleigh measurements temperature and absolute concentration of OH radical in strained diffusion flames. 8th International Symposium on Applications of Laser Techniques to Fluid Mechanics, Lisbon, Portugal

Rutland CJ; Ferziger JH (1991) Combust Flame 84:343-360

Samaniego JM; Mantel T (1999) Combust Flame 118:537-556

Shusser M; Gharib M; Mohseni K (1999) A new model for inviscid vortex ring formation. AIAA Paper 99-3805

Sung CJ; Kistler JS; Nishioka M; Law CK (1996) Combust Flame 105:189-201

Thévenin D; Renard PH; Fiechtner GJ; Gord JR; Rolon JC (2000) Proc Combust Inst 28:2101-2108

Watson KA; Lyons KM; Donbar JM; Carter CD (1999) Combust Flame 117:257-271

Watson KA; Lyons KM; Carter CD; Donbar JM (2002) Proc Combust Inst 29:in press

Figure Captions

Fig. 1. Schematic of the non-premixed counterflow vortex-flame burner

Fig. 2. Block diagram of the high-temporal-resolution synchronization scheme enabling imaging-vortex repeatability to within 10 μs

Fig. 3. Sequence of OH PLIF images with a temporal delay between images of 10 μs. Conditions are for Flame A (see Table 1) and incoming vortex convection velocity of 11.5 m/s

Fig. 4a, b. a Simultaneous OH-PLIF and velocity distributions for a case with no flame extinction; **b** superposed velocity and vorticity distributions. Conditions are for Flame C (see Table 1) and an incoming vortex convection velocity of 4 m/s. Images are 24.5 mm wide x 36 mm high, progress in time is from left to right, and images are spaced 9 ms apart

Fig. 5a, b. a Simultaneous OH-PLIF and velocity distributions for a case with flame extinction; **b** superposed velocity and vorticity distributions. Conditions are for Flame C (see Table 1) and an incoming vortex convection velocity of 5 m/s. Images are 24.5 mm wide x 36 mm high, progress in time is from left to right, and images are spaced 6 ms apart

Fig. 6. Simultaneous OH-PLIF and velocity distribution for Flame B (see Table 1) and an incoming vortex convection velocity of 8.25 m/s. Images are 24.5 mm wide x 36 mm high, progress in time is from left to right, and images are spaced 0.3 ms apart to show three stages of the extinction process. Symbols I-III represent regions located 0-10 mm along the flame front

Fig. 7a, b. a Velocity gradient normal to the flame surface (dU_n/dR) and the normalized OH fluorescence signal *along* the flame from Region I to III from the left-most image of Fig. 6; **b** velocity gradient normal to the flame surface measured *across* Regions I (centerline) and II (annular region) from the left-most image of Fig. 6

Table Captions

Table 1. Flow rates (LPM) at 21.5 °C and 724 mmHg for the three flames studied in the current investigation. $X_{H2\text{-}in\text{-}N2}$ is the volume fraction of hydrogen in nitrogen diluent

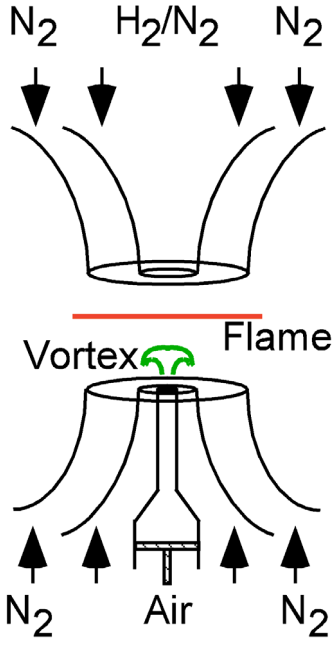

Fig. 1. Schematic of the non-premixed counterflow vortex-flame burner

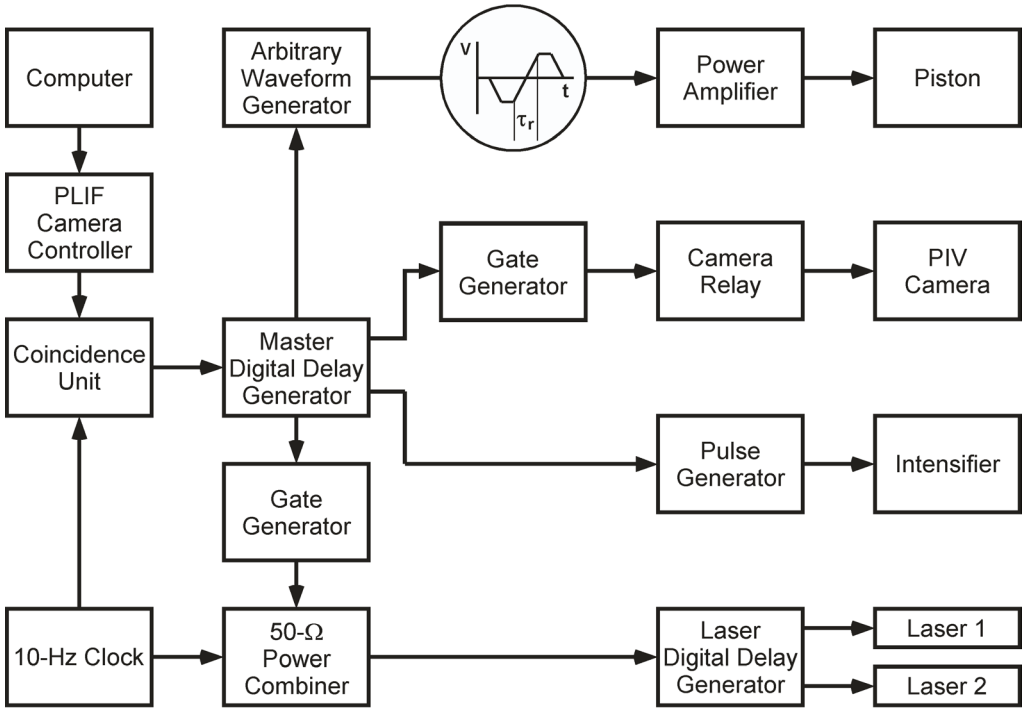

Fig. 2. Block diagram of the high-temporal-resolution synchronization scheme enabling imaging-vortex repeatability to within 10 μs

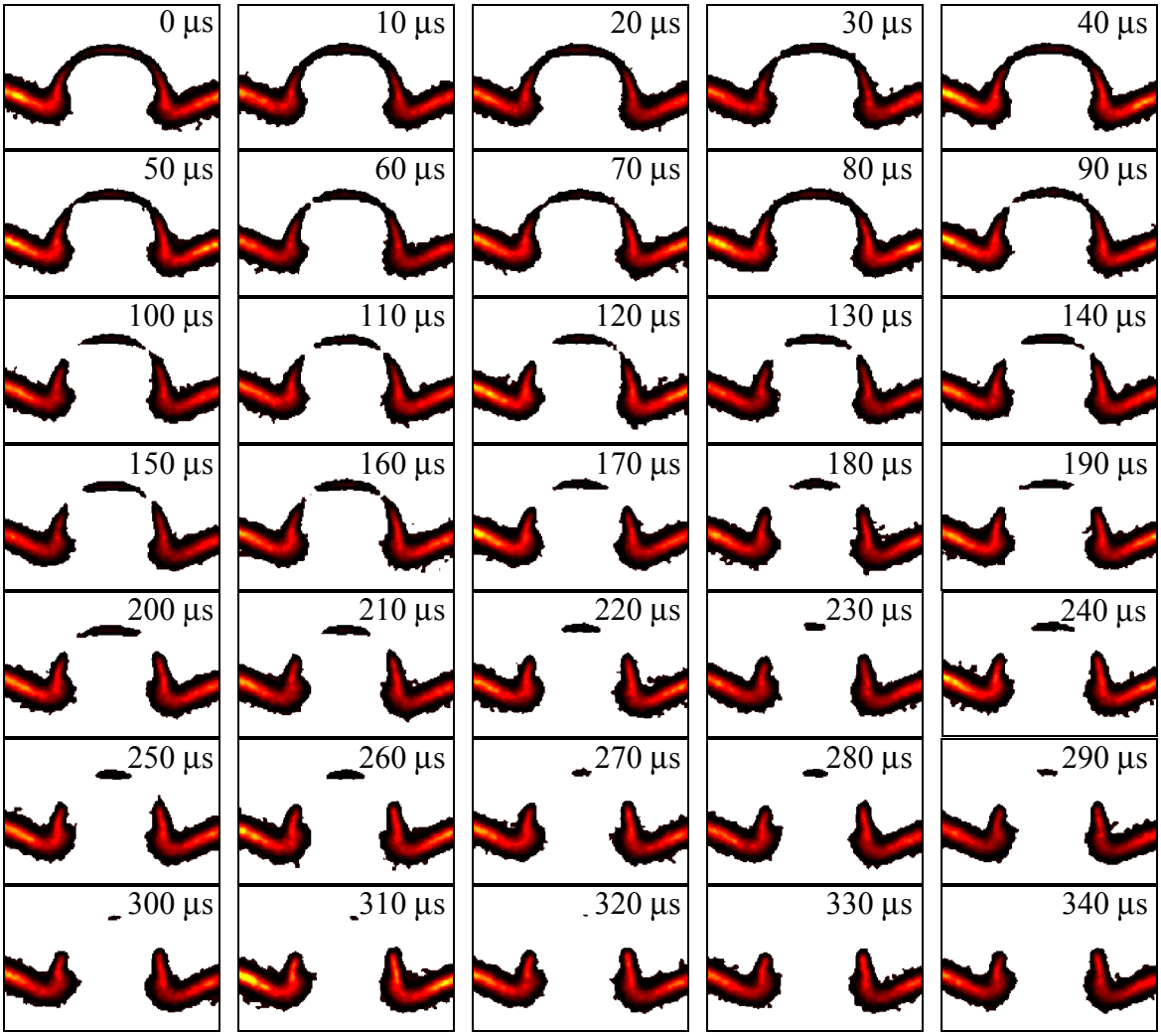

Fig. 3. Sequence of OH PLIF images with a temporal delay between images of 10 µs. Conditions are for Flame A (see Table 1) and incoming vortex convection velocity of 11.5 m/s

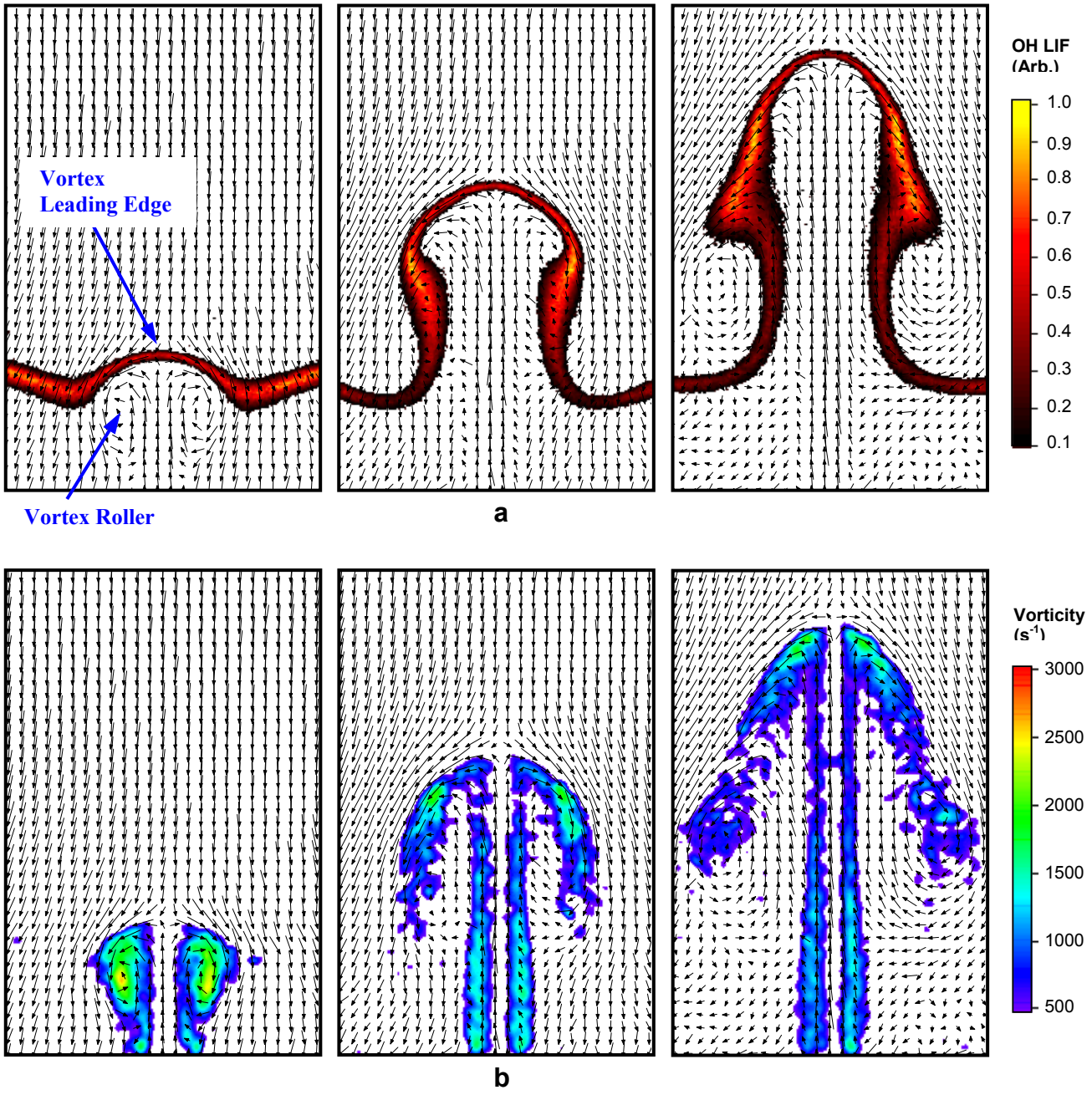

Fig. 4a, b. **a** Simultaneous OH-PLIF and velocity distributions for a case with no flame extinction; **b** superposed velocity and vorticity distributions. Conditions are for Flame C (see Table 1) and an incoming vortex convection velocity of 4 m/s. Images are 24.5 mm wide x 36 mm high, progress in time is from left to right, and images are spaced 9 ms apart

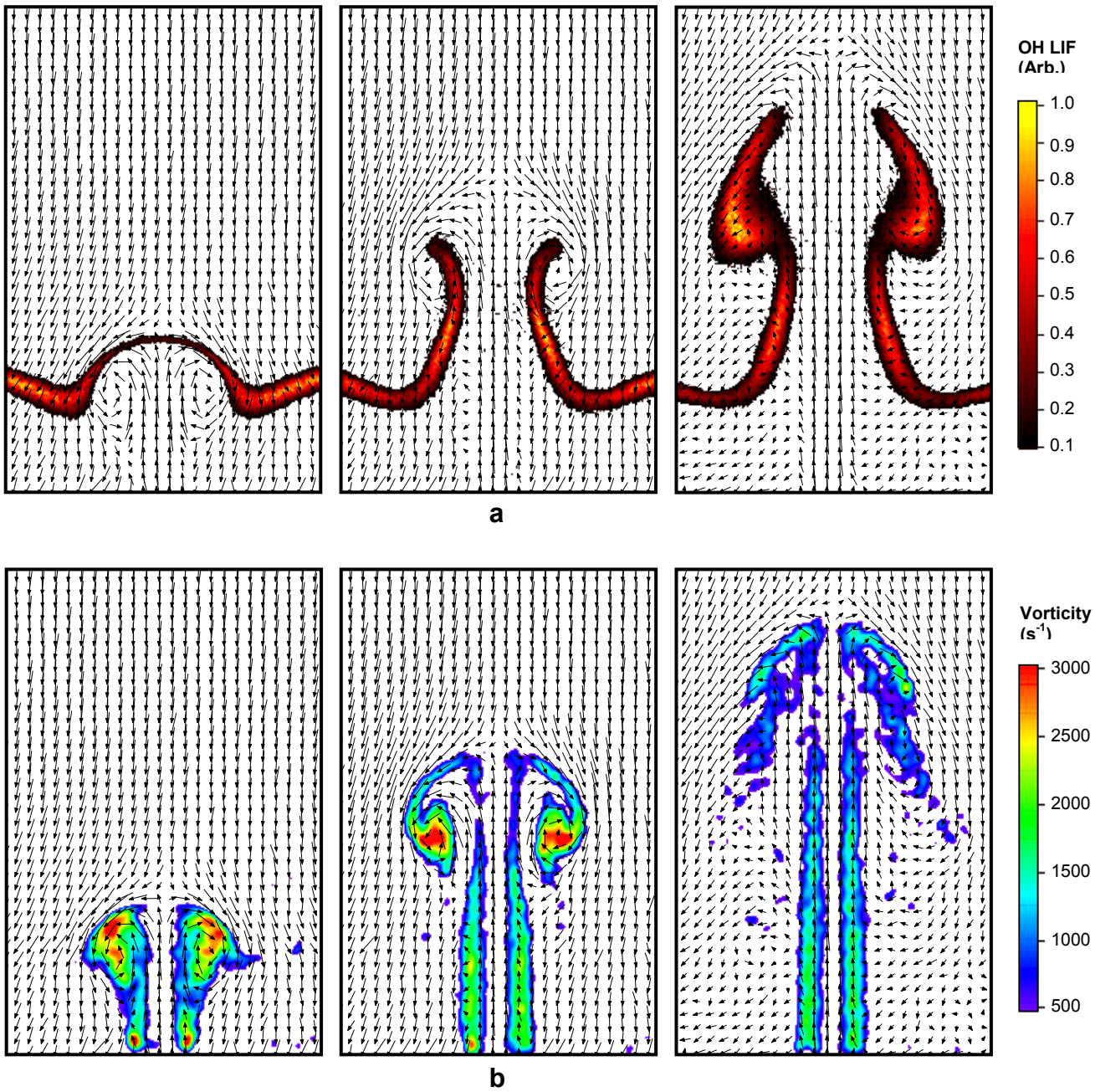

Fig. 5a, b. **a** Simultaneous OH-PLIF and velocity distributions for a case with flame extinction; **b** superposed velocity and vorticity distributions. Conditions are for Flame C (see Table 1) and an incoming vortex convection velocity of 5 m/s. Images are 24.5 mm wide x 36 mm high, progress in time is from left to right, and images are spaced 6 ms apart

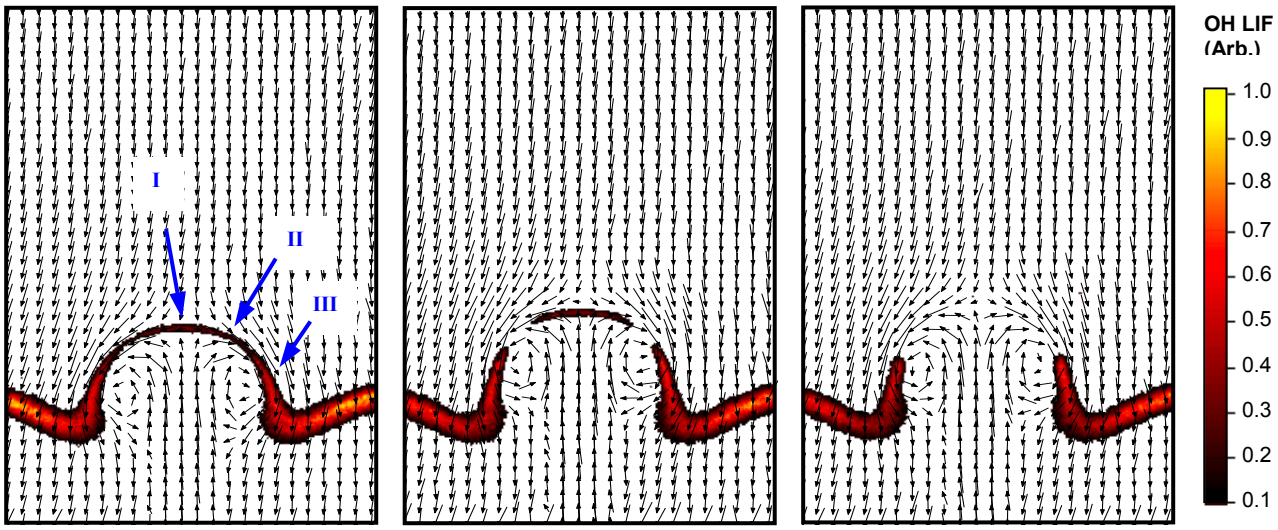

Fig. 6. Simultaneous OH-PLIF and velocity distribution for Flame B (see Table 1) and an incoming vortex convection velocity of 8.25 m/s. Images are 24.5 mm wide x 36 mm high, progress in time is from left to right, and images are spaced 0.3 ms apart to show three stages of the extinction process. Symbols I-III represent regions located 0-10 mm along the flame front

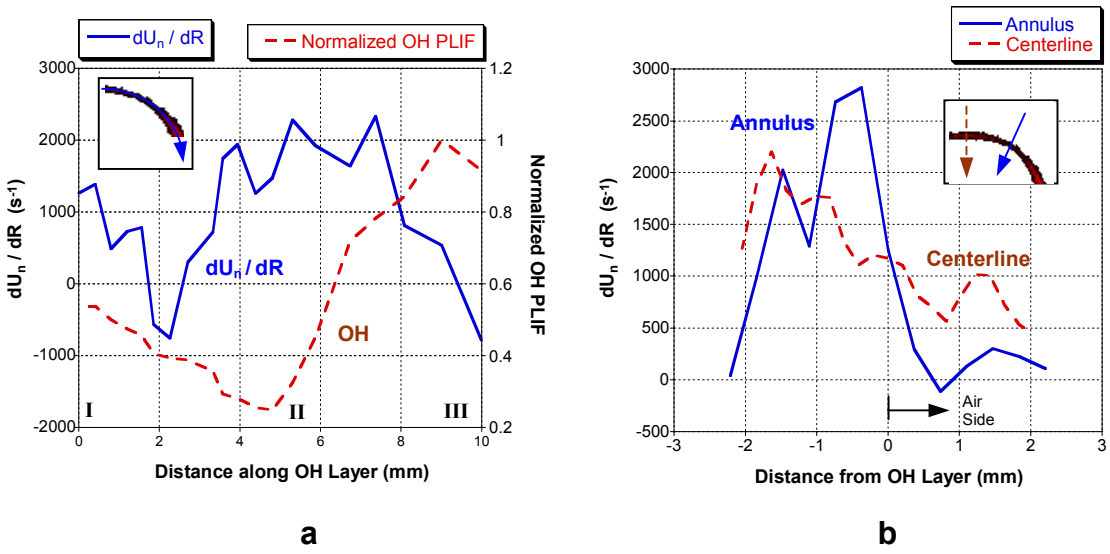

Fig. 7a, b. a Velocity gradient normal to the flame surface (dU_n/dR) and the normalized OH fluorescence signal *along* the flame from Region I to III from the left-most image of Fig. 6; **b** velocity gradient normal to the flame surface measured *across* Regions I (centerline) and II (annular region) from the left-most image of Fig. 6

Table 1. Flow rates (LPM) at 21.5 °C and 724 mmHg for the three flames studied in the current investigation. $X_{H2\text{-}in\text{-}N2}$ is the volume fraction of hydrogen in nitrogen diluent

Gas	Flame Type A	Flame Type B	Flame Type C
H_2 (SLPM)	5.31	4.67	4.04
N_2 Diluent (SLPM)	17.0	17.0	17.1
$X_{H2\text{-}in\text{-}N2}$	0.24	0.22	0.17
Air (SLPM)	11.2	11.2	11.2